The Effect of Linker DNA on the Structure and Interaction of Nucleosome Core Particles

Yen-Chih Huang,[†] Chun-Jen Su,[‡] Nikolay Korolev[§], Nikolay V. Berezhnoy[□,§], Sai Wang[§], Aghil Soman[§], Chun-Yu Chen,[‡] Hsin-Lung Chen,[*,†] U-Ser Jeng,[‡] and Lars Nordenskiöld[*,§]

[†]*Department of Chemical Engineering and Frontier Research Center on Fundamental and Applied Sciences of Matters, National Tsing Hua University, Hsin-Chu 30013, Taiwan*

[‡]*National Synchrotron Radiation Research Center, Hsinchu Science Park, Hsinchu 30076, Taiwan*

[§]*School of Biological Sciences, Nanyang Technological University, 60 Nanyang Drive, Singapore 637551, Singapor*e

[□]*Singapore Center for Environmental Life Sciences Engineering, Nanyang Technological University, 60 Nanyang Drive, 637551, Singapore*

*To whom correspondence should be addressed:

HLC: hlchen@che.nthu.edu.tw

LN: LARSNOR@ntu.edu.sg

Abstract

In eukaryotes, the compaction of the chromatin fibers composed of nucleosome core particles (NCPs) connected by linker DNA into chromosomes is highly efficient; however, the underlying folding mechanisms remain elusive. We used small angle X-ray scattering (SAXS) to investigate the influence of linker DNA length on the local structure and the interparticle interactions of the NCPs. In the presence of the linker DNA of 30 bp or less in length, the results suggest partial unwrapping of nucleosomal DNA on the NCP irrespective of the linker DNA length. Moreover, the presence of 15 bp linker DNA alleviated the electrostatic repulsion between the NCPs and prevented the formation of ordered columnar hexagonal phase, demonstrating that linker DNA plays an active role in chromatin folding.

Introduction

In most eukaryotes, genomic DNA is packed by nuclear proteins into chromatin, that consists of linear arrays of nucleosomes [1]. The nucleosome consists of the nucleosome core particle (NCP), formed by 147 bp DNA wrapped as a 1.75-turn super-helix around a histone octamer (HO), and linker DNA of variable length connecting neighbouring NCPs. The HO is made of two copies of each of the four core histone proteins H2A, H2B, H3 and H4 [2-5]. Each core histone has an unstructured, flexible and positively charged N-terminal domain, called the "histone tail" [6,7]. At the level of nucleosome array, chromatin resembles a 10-nm fibre termed "beads-on-a-string" [8,9]. At the next level of DNA packaging, linker histones bind linker DNA and nucleosome to further compact the 10-nm fibre into a 30-nm chromatin fibre [10-12] and higher-order structures in chromosomes [13]. Arrangement of chromatin fibers into loops leads to the formation of topologically associated domains that represent active and inactive chromatin regions of a single chromosome [14]. Although the existence of the 30-nm chromatin fibres in human mitotic chromosomes is disputed [15], the 30-nm fibres have been observed *in vivo* [16,17].

The NCP is a polyanion-polycation complex with a net charge of about −148e, consisting of negatively charged central particle (−236e, with charge of −294e from DNA and +58e from the globular part of the HO), to which eight flexible and positively charged N-terminal tails are attached (with net charge +88e) [18,19]. *In vitro*, the tails associate electrostatically with the DNA of its own NCP or facilitate interactions with nearby nucleosomes during chromatin compaction into the 30-nm fibre by electrostatic interactions and bridging [20-24]. Besides the electrostatic interactions, driven by the entropic gain from the release of counterions, that is primarily responsible for the stability of nucleosome, additional stabilization of the NCP comes from hydrogen bonding between the HO core and the DNA. Also, DNA being a stiff polymer with a 50 nm persistence length under physiological conditions, experiences a significant

conformational stress forming the nucleosome. However, unfavourable contribution of the DNA bending energy to nucleosome formation is overwhelmingly compensated by electrostatic interactions and hydrogen bonding, so overall the nucleosome and chromatin in general is a very stable DNA-protein complex [18].

The nucleosomes are known to be dynamic with up to 20% of the particles being in the unwrapped state according to FRET measurements [25]. The dynamic DNA unwrapping, termed "DNA breathing" may involve up to 40 bp of DNA from each site, corresponding to loss of DNA contacts primarily with the H2A-H2B dimers. The length of the unwrapped DNA is inversely proportional to the unwrapping frequency. The dynamic unwrapping of DNA is an essential part of the nucleosome (dis)assembly process taking place during DNA replication, transcription, repair and recombination [26]. Intermediates with unwrapped DNA from one or both entry/exit sites were also reported in MNase-seq studies on *Drosophila* chromatin *in vivo* [27]. Furthermore, the unwrapping of DNA in a condensed chromatin fibre was suggested to alleviate the DNA bending strain, based on force spectroscopy measurements [28] and from the accessibility of restriction enzymes [29].

The interaction between NCPs has been studied experimentally [30,31] and theoretically [24,32-35]. By controlling the ionic strength of the aqueous medium [20,30,31,36,37] and the NCP concentration [38], NCPs were found to behave as charged particles exhibiting repulsive interaction at low ionic strength, and forming multiple liquid crystalline phases under macromolecular crowding conditions or in the presence of multivalent cations of charge +2 and higher [20,21,23,31,36,37,39,40]. This behaviour of NCPs and nucleosome arrays [19,22,41-43] highlights the importance of an electrostatic mechanism in the compaction of chromatin due to its polyelectrolyte nature [19,44].

Small angle X-ray scattering (SAXS) studies of the solutions under the conditions of low monovalent salt where the NCPs repel each other and remain soluble, have been used to obtain

information on the shape, size and on the inter-particle interactions [23,31,36,38,45-49]. The shape of the NCPs and their interactions were affected by histone tail modifications, where a section of the nucleosomal DNA of ca. 20 bp in length unwrapped from the HO when the histone H3 and/or H4 tails were truncated [23,38,48].

Under the conditions of sufficient screening of the NCP charge, NCP-NCP interaction becomes attractive and relatively flat wedge-shaped NCP cylinders attach to each other by the flat surfaces forming columns of stacked NCPs. The NCP stacking has been experimentally observed in NCP crystals [2,50,51], in NCP liquid crystalline phases [30,37], in the crystal of the tetranucleosome [52], in folded nucleosome arrays [11,12,53], and in cryo-microscopy images of isolated native chromatin [54,55]. Therefore, nucleosome stacking is a universal feature of condensed NCPs and chromatin [56].

While the interactions of NCPs in solution have been studied, the role of linker DNA in the interaction between the NCPs was not systematically addressed despite being crucial for the folding of chromatin into the 30 nm fiber [13,57,58]. Studies on nucleosome conformational dynamics by van Noort and colleagues using spFRET revealed that DNA unwrapping is increased by higher monovalent salt concentrations, linker DNA length, and neighboring nucleosomes [59,60]. The present study focuses on the shape of nucleosome particles and the structures mediated by the inter-particle interactions of NCPs with linker DNA of defined lengths. We report the effects of the linker DNA length on the structure and inter-particle interactions of NCPs studied by solution SAXS. Three effects of the linker DNA were observed here: 1. unwrapping of nucleosomal DNA; 2. reduction of the electrostatic repulsion between NCPs; and 3. loss of the long-range ordered columnar hexagonal phase of NCPs in the presence of divalent cations. Effects 2 and 3 are particularly relevant to the chromatin fiber folding, which involves close contact of the negatively charged NCPs.

Materials and Methods

Preparation of nucleosomes

The DNA templates of 145, 157, 177 and 207 bp length with central 145 bp being '601' Widom nucleosome-positioning sequence [61] were used for nucleosome reconstitution (DNA sequences are given in the SI). The DNA constructs inserted in the pUC19 plasmid were amplified in *E. coli* HB101 strain, extracted by alkaline lysis method, released by EcoRV and separated by precipitation with PEG 6000 as described in our earlier work [31]. Recombinant *X. laevis* and *H. sapiens* core histone proteins H2A, H2B, H3 and H4 were expressed in *E. coli* [BL21 (DE3) pLysS] strain followed by separation of inclusion bodies and purification by gel-filtration and cation-exchange chromatography. The histone octamers (HO) were refolded by dialysis from the mixture of wild-type core histones H2A, H2B, H3 and H4 and purified by gel-filtration chromatography as described [42,62]. The purity and completeness of the HO refolding was checked by 18% SDS-PAGE. The NCP-145 were reconstituted using 145 bp DNA and the HO assembled from *X. laevis core histones*, whereas NCP-157, NCP-177, and NCP-207 were reconstituted, respectively, using 157 bp, 177 bp and 207 bp DNA templates and human HOs by a stepwise dialysis from a high- to low-salt buffer [63-65]. The quality of the reconstitution was assayed by 5% PAGE **(Figure S1** of the Supplementary Information**)**. The term NCP will be used for all histone - DNA constructs followed by the DNA length, NCP-145, NCP-157, NCP-177, and NCP-207. In all samples used in this work, background concentration of salt was 10 mM Tris pH 7.5, 10 mM KCl, 1 mM EDTA.

Small Angle X-ray Scattering (SAXS) data collection and analysis

SAXS experiments were carried out at the BL23A at National Synchrotron Radiation Research Center, (Hsinchu, Taiwan) [66] using PILATUS 1 M detector at the X-ray wavelength, λ, of 0.8266 Å and the sample-to-detector distance of 3083 mm. The scattering profiles of

NCPs and nucleosome in buffer were collected at room temperature (ca. 25° C). All scattering intensity profiles *I(q)* were displayed as a function of scattering vector, q, with $q = 4\pi\sin(\theta/2)/\lambda$ (θ = scattering angle).

Results of the SAXS measurements were analyzed using the ATSAS program package (version 2.8.2) [67,68]. The setting of this software presumes quality checks according to the recent guidelines for SAXS data analysis and presentation [69] and includes a search for optimal data range in the calculations of the radius of gyration R_g (from Guinier plot and from *P(r)* distribution), in the estimation of the maximal particle diameter (D_{max}), and in the fitting of form factors calculated from the molecular structures to the experimental SAXS profiles. Examples of Guinier and Kratky plots are given in the Supplementary Information (**Fig. S3** of the Supplementary Information).

Reference molecular structures used for calculating the form factors were generated from the published crystal structures of the 145 bp NCP with '601' positioning sequence 3LZ0.pdb [51] and from the NCP structure generated in all-atom molecular dynamics (MD) simulations using 1KX5.pdb [3] as a starting model. The MD-generated structure differs from the initial crystal structure by having basic histone tails collapsed on the negatively charged DNA, thus closely resembling the NCP in solution. Molecular models for NCP-157, NCP-177 and NCP-207 were obtained by attaching the straight B-form DNA with length and sequence matching the experimentally studied NCPs. The molecular structures of straight DNAs were generated by the NAB program [70]. To model unwinding of the DNA from the histone core in the NCPs, selected numbers of the DNA base pairs in the NCP (either 3LZ0.pdb or MD-generated) were replaced by stretches of straight B-form DNA of the same sequence from one or both ends of the NCP. Explicit hydrogen atoms were added to the crystal structures. The Chimera molecular manipulation and visualization package was used for generation of the structures [71].

The scattering profiles were fitted by the product of the structure factor associated with the

screened Coulomb potential [72] which describes the interaction between NCPs and the experimentally observed form factor of NCP-145 and NCP-177 [73].

The CRYSOL module of the ATSAS package was used to fit experimental and simulated profiles and estimate quality of the fitting. The spectra were analyzed in the q range from 0.01 to 0.3 $Å^{-1}$for the NCP-145; the fitting q range was from 0.05 to 0.25 $Å^{-1}$for the NCP-157, NCP-177 and NCP-207,.

Results and Discussions

Interpretation of the form factor scattering of NCP-145, NCP-157, NCP-177 and NCP-207 using atomistic models

The experimental SAXS profiles of the NCPs with various DNA lengths (145, 157, 177 and 207 bp) in low-salt buffer solution at low NCP concentration are shown in **Fig. 1A**. The scattering curves were analyzed using the particle form factors based on the atomistic structure of the NCP-145 with addition of straight B-form DNA attached at the entry and exit sites for modeling the linker DNA lengths and unwrapping. The experimental SAXS profiles were interpreted based on the quality of the fit of the form factors calculated from these model structures to the experimentally observed SAXS profiles and by fitting-derived particle parameters including R_g and D_{max} to be defined later.

The solution SAXS profiles of NCP-145 and the nucleosomes with linker DNA (i.e., NCP-157, NCP-177 and NCP-207) appeared comparable (**Fig. 1A**); however, the characteristic dip around q = 0.14 $Å^{-1}$ in the spectrum of NCP-145 became progressively shallower with increasing linker DNA length (**Fig. 1B**). Similar effects in the form factor profile have been observed for the NCPs derived from natural source (i.e. the sequence of the nucleosomal DNA was not the Widom 601 sequence) as well as for NCPs with truncated or chemically modified histone tails [23,31,38,45,48]. For the NCPs with the same DNA length, the decrease in the depth of

the dip around q = 0.14 $Å^{-1}$ was attributed to the partial unwrapping of the nucleosomal DNA, and the scattering profile changes were reproduced in the simulated SAXS spectra using the NCP structures modeling DNA unwrapping [23,38,45,48]. The partial unwrapping of the nucleosomal DNA is likely to alleviate the repulsion between the two arms of linker DNA (see sketches of the NCP-157, NCP-177 and NCP-207 structure in row (A) of **Fig. 2**). However, the scattering intensity response induced by the form factor change due to the increase of linker DNA length was not studied earlier and needs to be considered.

Atomistic models allow the separation of the effect of the linker DNA from that of the unwrapping of nucleosomal DNA on the form factor of the NCPs. Two variants of the NCP-145 structure were used to calculate SAXS profiles. One structure was based on a snapshot from an all-atom MD simulation of the 147 bp (truncated to 145 bp) α-satellite NCP (1KX5.pdb), where the histone tails, which are included explicitly in the established structure, are collapsed on the DNA (**Figure S2A** of the Supplementary Information). Another NCP structure corresponds to the published pdb structure of the NCP with 145 bp DNA of the '601' sequence (which was used in the experiments) (3LZ0.pdb), where a significant portion of the histone tails is missing (**Fig. S2B** of the Supplementary Information). Both structures were used to model the unwrapping of a certain number of DNA base pairs from the entry and exit sites. The form factor from the MD-generated structure [19] was found to result in a higher fit quality of the experimental SAXS profiles, compared to the one from the published '601' crystal structure having parts of the tails missing (**Fig. S2** and **Table S1** of the Supplementary Information). A few models with DNA unwrapping led to comparable fit quality for the MD-generated models and improved fit quality for the crystal structure models. The modeling demonstrated that, while the DNA sequence has no apparent influence on the form factor, the fit quality can be improved by the presence of all histone tails bound to the nucleosomal DNA and by including DNA unwrapping. Consequently, the MD-generated NCP structure was used

to build the atomic structures for modeling DNA unwrapping for the other NCPs with linker DNA (**Fig. 2**).

The radii of gyration R_g determined from the Guinier regions in the experimental SAXS profiles for NCP-145, NCP-157, NCP-177 and NCP-207 were about 43, 45, 47 and 55 Å, respectively (**Tables S1-S4** and **Fig. S3** of the Supplementary Information). The distance distribution function, *P(r)*, which allows the determination of the maximal intra-atom distances within a particle (D_{max}), from the experimentally observed SAXS profiles, was also calculated for NCP-145, NCP-157, NCP-177 and NCP-207 to be 140, 144, 173 and 205 Å, respectively (**Fig. 3**). Both independent types of analysis indicate an increase of the effective particle size with increasing linker DNA length. The SAXS curves simulated for NCP structures with different unwrapping lengths of the nucleosomal DNA were analyzed using the same approach.

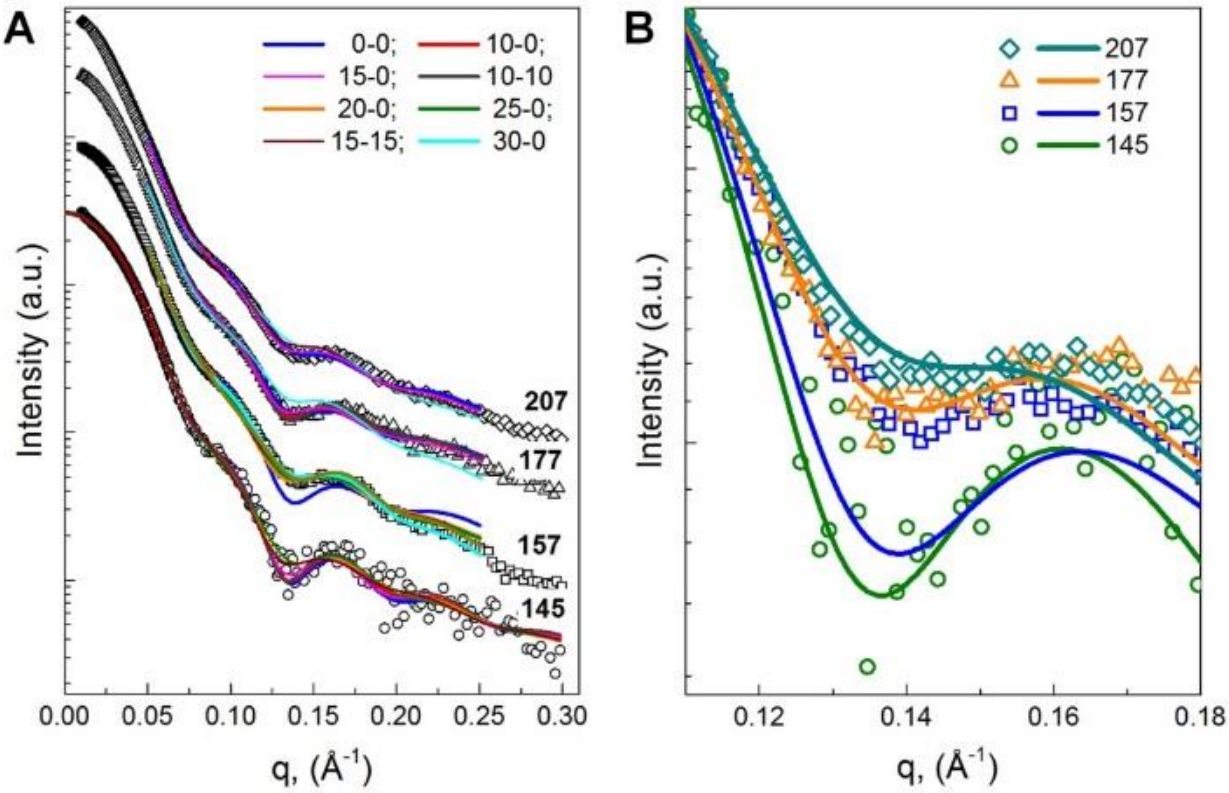

Fig. 1. Comparison of SAXS profiles measured experimentally (points) and those calculated from molecular structures (curves). (A) Full range of the results. Experimental data are for the NCP-145 (1.25 mg/mL), NCP-157 (3 mg/mL), NCP-177 (1.5 mg/mL), and NCP-207 (3 mg/mL) as indicated in the graph by the number of the DNA base pairs. Different curves superposing on a given experimental SAXS profile were calculated from the molecular structure model with different unwrapping lengths of DNA from one or two ends of the NCPs. (B). The region around q = 0.14 $Å^{-1}$ where characteristic local minimum is observed. The curves correspond to the form factors calculated for the model nucleosome structures without DNA unwrapping (0-0 curves in graph A). The number of the DNA base pairs in the nucleosome is indicated in the figure. See text for details.

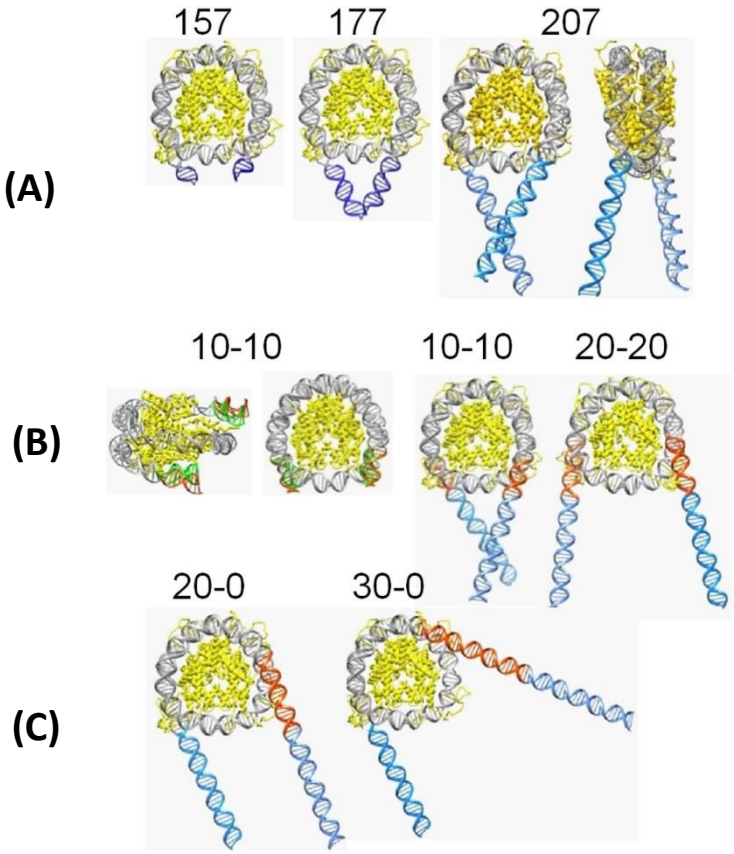

Fig. 2 Examples of the nucleosome model structures. Row (A): NCP-157, NCP-177 and NCP-207 structures generated by the addition of respectively 5, 15 and 30 bp of straight B-DNA double helix to the 147 bp NCP structure obtained in the MD simulation initiated from 1KX5 crystal structure. For the NCP-207, two projections of the structure (top and side views) are shown to show separation between stretches of linker DNA. Row (B) and (C) show examples of the NCPs with partially unwrapped DNA. Stretches of the DNA detached from the histone core are shown in orange; linker DNA is in blue. The two structures to the left in row (B) represent superposition of the two NCP-145 structures, one is intact 3LZ0 10 bp at each end shown in green; the other is a model with 10 bp DNA (shown in red) unwrapped from entry and exit. The other structures in the row (B) and (C) are NCP-207 with symmetric (10-10 and 20-20) and asymmetric (20-0 and 30-0) DNA unwrapping from the histone core. See text for details

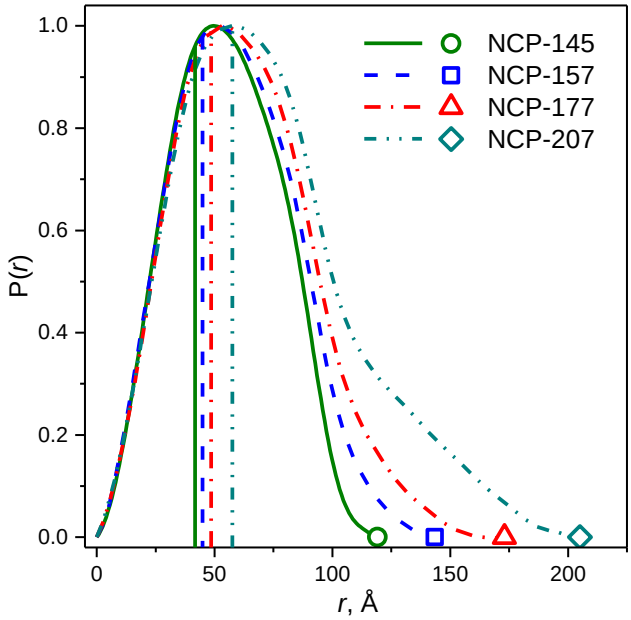

Fig. 3. Comparison of the distance distribution functions P(*r*) calculated from the solution SAXS profiles of NCP-145 (1.25 mg/mL), NCP-157 (3 mg/mL), NCP-177 (1.5 mg/mL), and NCP-207 (3 mg/mL). Vertical lines indicate the values of the corresponding R_g. The points locate the values of D_{max} (maximal pair distance) of each NCP type.

The calculated scattering curves of NCP-145 with the unwrapping lengths of up to 20 DNA bp, both symmetric or asymmetric, fitted well the experimental spectrum with a characteristic dip at q = 0.14 Å^{-1} (**Fig. 1**); moreover, the experimentally determined R_g and D_{max} values were better reproduced by the models with an unwrapping length up to 20 bp (**Fig. S4** and **Table S1** of the Supplementary Information). The models with an unwrapping length greater than 20 bp yielded worse fitting, with respect to the reduction of the dip depth and gave R_g and D_{max} values that deviate from the experimental ones. These results suggest that the nucleosomal DNA with the Widom '601' sequence in NCP-145 experiences an unwrapping of up to 20 bp in solution, and that the majority of the DNA remains tightly wrapped around the HO, as predicted by the crystal structure and confirmed in other studies [31,36,45]. Visual comparison of the NCP-145 structures with various degrees of the DNA unwrapping confirms that unwrapping of up to 20

bp from the histone core does not cause significant changes of the NCP structure (see the 2 snapshots on the left of the row (B) of **Fig. 2**), as similar SAXS profiles were obtained. This observation is in agreement with structural analysis that has shown 129 bp of the DNA being tightly wrapped around the HO core, in contrast to the 6-9 bp at the NCP entry and exit being less bent [56,76].

For the NCP-157, NCP-177 and NCP-207, the structure models with unwrapping up to 20 bp were found to produce the scattering curves with a reasonable fit to the experimental SAXS profiles and particularly R_g and D_{max} values that were consistently closer to the experimentally determined values as compared to the fully wrapped models (**Fig**. **1A** and **Fig. S4** of Supplementary Information). Overall, the reasonable agreement between the experimental SAXS profiles and the form factors calculated for a number of NCP structures in which the DNA shows moderate unwrapping from the HO argues in favor of variable nucleosome structure with dynamic but limited breathing of the DNA ends that may be somewhat enhanced in the presence of linker DNA. Previous FRET studies using 10 times longer linker DNA (30 bp vs 300 bp) reported up to 3 times increase in the fraction of nucleosomes with unwrapping [59]. The present work shows that the linker DNA of up to 30 bp did not significantly influence the degree of DNA unwrapping, and the change of the SAXS pattern, in particular the depth decrease of the dip at 0.14 $Å^{-1}$, with the increase of linker DNA length was due mainly to the excess intensity contributed by the linker DNA.

It is noted that here we compared the experimental SAXS profiles with the form factors of the static NCP models; a more realistic description of the NCPs in solution is a dynamic ensemble where fully folded NCPs co-exist with the structures where DNA is partially detached from the histone core. Hence, in the solution of non-interacting particles, the experimental SAXS profile represents the population-averaged sum of the form factors of all possible NCP structures. Recently, the ensemble optimization method (EOM) has been developed and

elaborated fitting procedures were applied to fit the experimental SAXS profile to a combination of theoretical spectra calculated from a pool of all possible molecular structures for a given particle. In particular this method was applied to study DNA unwrapping from the NCPs [74,75]. However, we think that the analysis based on fitting of a single calculated form factor to the experimental spectrum is a reasonable approach, as it gives a sound estimation of the NCP structure that constitutes the major fraction in the ensemble. It is also plausible that the linker DNA detached from the HO is rather straight and close to the idealized B-form DNA, at least at the level of the structural resolution of the SAXS spectra in solution.

Linker DNA reduces the electrostatic repulsion between nucleosome particles

The NCP is a polycation-polyanion complex bearing a net negative charge. In aqueous medium at low salt concentration, the interactions between NCPs are electrostatically repulsive, but in the presence of multivalent cations it becomes attractive due to ion-ion correlation and tail bridging effects [19]. It was previously shown that the NCP interparticle interactions under low salt condition could be qualitatively described using a screened Coulomb potential to interpret the solution SAXS spectra [20,38]. We followed this approach here to reveal the difference in the strength of the interparticle interactions between NCP-145 and NCP-177 using the solution SAXS profiles collected at various particle concentrations. **Fig. 4A** and **4B** display the SAXS profiles as a function of NCP concentration under low salt conditions for NCP-145 and NCP-177, respectively. The scattering profiles in the q region 0.03 - 0.04 $Å^{-1}$ remained virtually unchanged with respect to the variation of concentration for both systems, indicating that the local structure of the nucleosome particles was unperturbed. Nevertheless, the scattering curves of NCP-145 in the low-q region ($q < 0.03$ $Å^{-1}$) gradually deviated from the Guinier's law as the concentration increased, signaling that the interparticle interactions became significant at sufficiently high NCP concentration. At the highest concentration studied, i.e. 17 mg/mL, the low-q intensity exhibited an apparent downturn

arising from the repulsion between NCPs [38,72,77]. For NCP-177 the concentration-dependent change of scattering intensity in the low-q region was less pronounced, compared to NCP-145, indicating a weaker interparticle repulsion of NCP-177 under a given concentration.

To resolve the difference in interparticle interaction between the two systems more clearly, we have further obtained the structure factors of NCP-145 and NCP-177 at various concentrations by dividing the intensity profiles by their respective form factors. The structure factors thus obtained are displayed in **Fig. S5** of the Supplementary Information. It can be seen that, over the concentration range studied, the structure factor of NCP-145 displayed a much more pronounced concentration dependence and deviation from the value of 1.0 in the low-q region than that of NCP-177, conforming that NCP-145 exhibited a stronger interparticle interaction than NCP-177 under a given concentration.

It is noted that the SAXS intensity profile in the low-q region of NCP-145 at 2.5 mg/ml deviated from that at 1.25 mg/ml which corresponds to the form factor of NCP-145 according to **Fig. 1** (see the inset of **Fig. 4A**), indicating non-negligible interparticle interaction at 2.5 mg/ml. On the other hand, the SAXS profile of NCP-177 at 3 mg/ml overlapped nearly perfectly with that collected at 1.5 mg/ml (which corresponds to the form factor of NCP-177 according to **Fig. 1**), showing that the interparticle interaction of NCP-177 at 3 mg/ml was essentially negligible. The SAXS curves of NCP-157 and NCP-207 in **Fig. 1** were both collected at the concentration of 3 mg/ml; the fact that the observed profiles of these two samples matched very well with those calculated by the corresponding form factors (i.e., the solid curves in **Fig. 1**) attests that the interparticle interaction of these two NCPs was also negligible at 3 mg/ml. This finding along with the results (i.e., **Fig. 4B**) obtained from the systematic variation of the concentration of NCP-177 demonstrated unambiguously that the presence of linker DNA alleviated the electrostatic repulsion between NCPs in the solution

irrespective of the length of linker DNA.

To obtain an approximate assessment of the change of electrostatic repulsion in quantitative terms, the observed SAXS profiles were fitted by calculating the structure factor following the approach by Hayter and co-workers, based on a charge normalization procedure [72,78], coupled with the form factors of the nucleosome particles given by the corresponding SAXS curves observed at the lowest concentration. The structure factor was calculated based on the screened Coulomb potential using the effective particle charge and the effective particle diameter as the variable fitting parameter under the given condition of particle concentration and ionic strength (defined by the KCl concentration of 10 mM). Once the effective charge and the effective diameter of NCP-145 and NCP-177 were obtained from the fitting results of the scattering curves associated with the respective highest NCP concentrations (i.e. 17 and 12.4 mg/mL for NCP-145 and NCP-177, respectively), these two parameters were then fixed for the subsequent fittings of the scattering curves with more dilute NCP concentration; in this case, the volume faction of the NCP became the remaining variable of the fittings. The fitted scattering curves were superimposed on the experimental data in **Fig. 4**, and the fitting parameters are listed in **Table 1.**

It is noted that the Debye-Hückel type of approach that underlies the present treatment for obtaining a screened Coulomb potential is defined for an ionic strength defined by the 10 mM KCl concentration of the buffer solution and the counterions neutralizing the NCP were neglected. In the second row of Table 1, the variation of the total ion concentration, including both the monovalent cations from KCl as well as the buffer ($Tris^+$) and the neutralizing counterions of the NCP-145 or NCP-177 are given. Even though such an approximation leads to underestimation of the screened potential, the qualitative conclusions described above are expected to remain valid.

As can be seen from **Table 1**, the fitting results revealed smaller effective charge of NCP-177 compared to that of NCP-145 at a given concentration. NCP-177 is composed of a 147 NCP and two 15 bp linker DNAs extended from the two ends of the nucleosomal DNA. Because the linker DNA and the 147 NCP are both negatively charged, the electrostatic repulsion between these two components could be significant due to their large effective charges and spatial proximity in the nucleosome. To alleviate this repulsive interaction, more counterions might condense on 147 NCP and linker DNA to reduce their respective effective charges, which in turn led to the smaller overall charge of NCP-177.

Another possible reason for the weaker interparticle interaction experienced by NCP-177 is the asymmetries in charge and particle geometry caused by the conformational fluctuations of the linker DNA around the NCP. The particles with polarity or asymmetry in charge may interact with one another to reduce their electrostatic repulsion, if the pair of the interacting particles adopt the proper orientation (e.g., the more negatively charged end of one particle faces toward the less negatively charged end of the other particle). Considering that the random conformational fluctuations of the linker DNA should be faster than the orientation adjustment of the particles, thus the reduction of the electrostatic repulsion might be frustrated, because the proper orientation between a pair of particles with a given transient shape may be difficult to attain before their shapes were changed again by the conformational fluctuations. As a result, the enhancement of the counterion condensation on NCP could be the more plausible explanation for the linker DNA-induced reduction of interparticle repulsion. Although the identification of the exact mechanism requires further study, our experimental results revealed that the linker DNA not only slightly facilitates the unwrapping of the nucleosomal DNA, but also alleviates the repulsive interaction between the NCPs. A possible implication of this effect is the facilitation of chromatin folding via reducing the repulsion between the neighboring NCPs in the fiber.

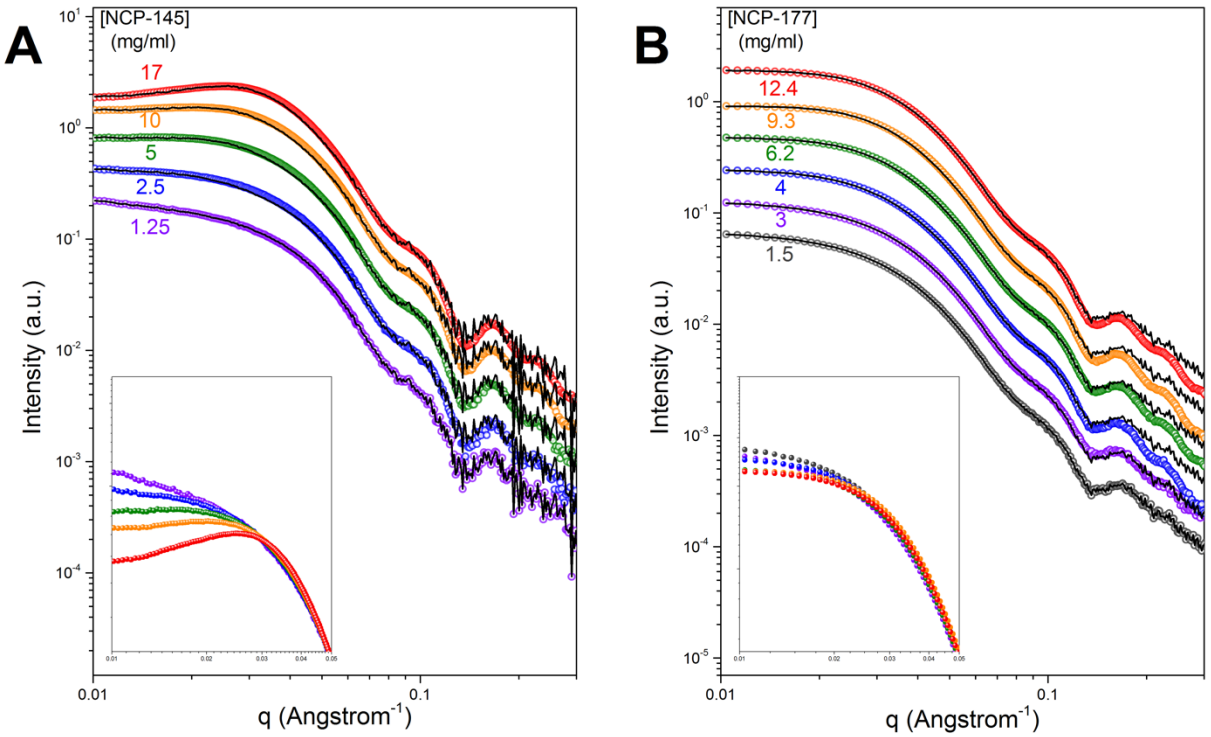

Fig. 4. Concentration effect on the structures and interparticle interactions in the solutions of (**A**) NCP-145 and (**B**) NCP-177 (NCP concentrations in mg/mL are indicated in the graphs). Experimental SAXS profiles (points) are superimposed with the fitting results (black curves) using the combination of the structure factor associated with the screened Coulomb interaction and the form factors of NCP-145 and NCP-177. The inserts show the SAXS profiles scaled in the q range from 0.05 to 0.25 Å^{-1} (to normalize the differences between the samples in concentrations and optical path) to highlight the changes in the low-q scattering relating to the interparticle interaction. The NCP-145 data was first published in [31].

Table 1. Parameters obtained from the fittings of the SAXS profiles of NCP-145 and NCP-177 using the combination of the structure factor associated with the screened Coulomb interaction and the form factors of the respective nucleosome particles given by the scattering profiles at the lowest concentrations (i.e. 1.25 mg/ml for NCP-145 and 1.5 mg/ml for NCP-177).

	NCP-145				NCP-177			
concentration (mg/ml)	17	10	5	2.5	12.4	9.3	6.2	4
Total cation concentration,	30.5	25.5	22.0	20.2	30.1	27.2	24.2	22.2

(mM)*								
diameter (Å)	96 ±0.63	96	96	96	125 ±4.82	125	125	125
effective charge (e)	31 ±0.90	31	31	31	15 ±2.02	15	15	15
volume fraction	0.020 $\pm 3x10^{-4}$	0.011 $\pm 3x10^{-4}$	0.007 $\pm 3x10^{-4}$	0002 $\pm 3x10^{-4}$	0.015 $\pm 1x10^{-3}$	0.016 $\pm 1x10^{-3}$	0.010 $\pm 1x10^{-3}$	0.005 $\pm 1x10^{-3}$

* Sum of the cation concentrations in the TEK buffer (10 mM K^+ + 8.4 mM $Tris^+$) and monovalent cations neutralizing net negative charge of NCP-145 or NCP-177

The presence of linker DNA abolishes the cation-induced formation of the NCP columnar hexagonal phase

Salt plays a crucial role in tuning the biological function and compaction of chromatin [30,36-38,79-83]. Divalent ions, like Mg^{2+} and Ca^{2+}, exert a stronger influence on the nucleosome structure and interaction than monovalent ions and were found to aid chromatin folding [39,40,82-84]. It is well known that the solutions of NCPs form a (mainly) columnar hexagonal phase under the influence of divalent Mg^{2+} as well as in the presence of higher valence cations like hexaamminecobalt(III) ($Co(NH_3)_6]^{3+}$), spermidine^{3+} and spermine^{4+} [30,31,37,39]. The supramolecular structure within a phase can be determined from the pattern of the Bragg peaks recorded using SAXS. Although the ordered phase of NCP in the presence of $CaCl_2$ was not previously characterized, based on precipitation assay studies [40], a solution of NCP-145 in the presence of this cation would, similar to the case of $MgCl_2$, be expected to form a columnar hexagonal phase, although this remains to be confirmed. However, the effect of the presence of linker DNA on the precipitated phase of NCPs is not known. Here, we have further investigated the effect of the presence of linker DNA on the interaction between nucleosome particles by studying the precipitated phases of NCP-145 and NCP-177 at variable $CaCl_2$ concentrations (as well as in the presence of $MgCl_2$).

Figure 5 presents the SAXS profiles of solutions of NCP-145 and NCP-177 as a function

of $CaCl_2$ concentrations. The NCP concentrations were 2.5 and 3 mg/mL, respectively, and according to the discussion above, the interparticle interaction in solution should be negligible. Upon increasing the divalent salt concentration in the NCP-145 solution to 3 mM, the intensity in the low-q region ($q < 0.025$ Å^{-1}) showed a strong upturn relative to the SAXS profile of the salt-free solution, as demonstrated more clearly in the inset of **Fig. 5A**. The intensity increase in the low-q region indicates the attraction between nucleosomes originating from electrostatic interactions and the histone tail bridging effect [20,24,31,32,34,38]. The SAXS profiles in the high-q region ($q > 0.1$ Å^{-1}) remained virtually unaffected by the salt addition, suggesting that the local structure of the NCP-145 was unperturbed at low divalent salt concentration ($\leq$ 3 mM). A similar alteration of the scattering pattern was observed for NCP-177 when the $CaCl_2$ concentration was increased up to 7 mM.

It is important to note that the perturbation of the SAXS profile induced by salt addition was less significant in NCP-177 (as demonstrated on the inset of **Fig. 5B**), suggesting that linker DNA imposed a hindrance to the ion-ion correlation disturbance and tail-bridging attraction. It may be further noted that the NCP-145 and NCP-177 spectra starting from 5 and 10 mM Ca^{2+}, respectively, appeared slightly different from the solution spectra at lower Ca^{2+} concentrations by having a higher relative intensity in the range of $q > 0.1$ Å^{-1}. At the $CaCl_2$ salt concentration of 5 mM and above, the SAXS profiles of NCP-145 exhibited a set of diffraction peaks characteristic of hexagonal packing of columns of stacked NCPs [31,37]. The peaks became sharper and stronger in intensity at higher salt concentration, indicating the enhancement of long-range order of the columnar hexagonal phase. Moreover, the intensity of the (11) peak of the hexagonal lattice was similar to that of the (10) peak, which may be ascribed to the overlap of the (11) peak with the correlation peak associated with the average interparticle distance between the NCPs along the column axis, which was about 56 Å. Unlike NCP-145, the scattering curves of NCP-177 solutions did not exhibit Bragg peaks in the same

concentration range and higher (i.e. 5 - 50 mM). Similar results were also observed for NCP-157 and NCP-207 with $CaCl_2$ addition (see **Fig. S6** of the Supplementary Information).

We also performed the SAXS measurements for NCP-177 in the presence of increasing concentrations of $MgCl_2$ and the results were similar to that obtained for $CaCl_2$ described above (the concentration range studied was somewhat different; see **Fig. S7** of the Supplementary Information). The NCP-177 concentration investigated in the $MgCl_2$ addition experiment was 8 mg/mL while that in $CaCl_2$ addition experiment was 3 mg/mL, and this higher particle concentration could form precipitation during salt addition. The precipitated NCP-177 particles also did not show the formation of the ordered columnar hexagonal phase under the influence of Mg^{2+} ions. However, as can clearly be seen from the data in **Fig. S7**, the scattering curves exhibit broad Bragg peaks characteristic of columnar stacking of few NCPs in the precipitated phase with no long range order [31].

It can also be noted that a well-known effect of the addition of divalent (and higher valence counterions) cations to NCP solutions is the phenomenon of resolubilization of the precipitated NCP phase forming an isotropic solution at higher concentrations of added cations. Precipitation assay studies showed this to occur at Mg^{2+}/Ca^{2+} concentrations higher than about 20 mM for NCPs having an average length of about 160 bp [39]. The appearance of the SAXS profile of NCP-177 at 50 mM Ca^{2+} may indicate interparticle interactions being repulsive, leading to the absence of NCP stacking.

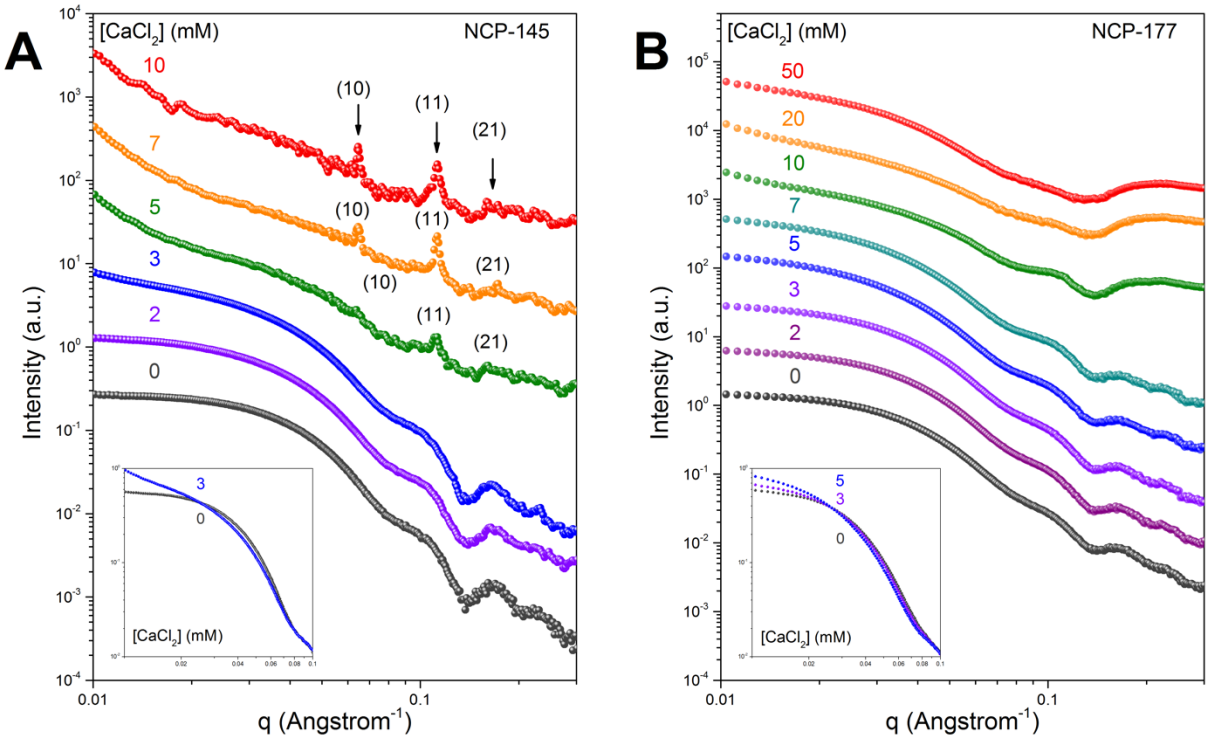

Fig. 5. Influence of $CaCl_2$ on the structures and interparticle interactions of the NCP-145 (**A**) and NCP-177 (**B**). Concentrations of added $CaCl_2$ (in mM) are indicated in the graphs. The initial NCP concentrations are 2.5 and 3 mg/ml for NCP-145 and NCP-177, respectively. The arrows in (**A**) identify the diffraction peaks associated with the hexagonal columnar phase. The inserts superimpose the SAXS profiles of the NCP-145 and NCP-177, to demonstrate the salt-induced change in low-q intensities

Conclusions

In summary, this study revealed that linker DNA influenced the local structure and interaction of nucleosome particles. By using pdb structure models of the NCP based on existing crystal structures with extension of the DNA at the entry-exit positions, we created detailed structural models of the NCP with variable linker DNA lengths and with different degrees of unwrapping of the nucleosomal DNA. These structures were then used to calculate the SAXS profiles for comparison with the experimental data (**Figs. 1 and 2**). For NCP-145, it was found that an NCP structures with no, 10 or 15 bp asymmetric unwrapping on one side, and symmetric unwrapping of 10 bp on both sides displayed a good fit to the experimental

curve. These observations suggest that the NCP in solution sampled a range of conformations with various degree of DNA unwrapping within these limits and perhaps even beyond, in agreement with other studies (Ref. [59] and the references therein) We compared the calculated form factors obtained for the MD generated structure with the tails collapsed onto the NCP with the SAXS profile generated from the structure in the pdb databank (for the '601' NCP-145) where most amino acids for the tails are missing. This comparison unequivocally showed that using a physically realistic structure with tails collapsed on the NCP gave a more realistic description of the solution structure. Alternatively, the exclusion of tails from the structure results in an inferior model, compared to the MD generated structure [31].

For NCPs with linker DNA, we found that all cases can be reasonably well described by a range of nucleosomal DNA unwrapping comparable to the NCP-145. In conclusion, the presence of linker DNA up to 30 bp did not significantly affect the nucleosome breathing, but influenced the particle shape.

It should be noted that a more rigorous prediction would be based on generating an ensemble of NCP structures with variable degrees of DNA unwrapping and calculating the form factor curve as an average from such an ensemble of structures. Unfortunately, the millisecond time scale for the DNA breathing [25] is much slower than what can be sampled in all-atom MD simulations. In fact, we found that the DNA almost does not move at all from the starting position during a 500 ns MD simulation (data not shown) and using any snapshot during such a trajectory would lead to almost identical SAXS curves as tails, albeit highly dynamic, stay collapsed on the NCP at all instantaneous time points. This observed dynamic unwrapping of nucleosomal DNA may be relevant to the movement of NCP along the chromatin fiber such as in NCP sliding.

Linker DNA also impacts the interparticle interaction of the nucleosomes as a function of concentrations of NCP and salt. The NCP-145 exhibited a screened Coulomb interaction in the

aqueous medium with low salt concentration. However, on the contrary, though screened Coulomb interaction was still operative, the NCP-177 was found to carry less effective charge than the NCP-145, likely caused by the presence of linker DNA that induced a significant counterion condensation to alleviate the repulsion between the NCP and the linker DNA extended from it.

Figure 6 shows the schematic illustration of the divalent calcium-salt effect on the structure of the nucleosome systems. In agreement with previous observations for Mg^{2+} [31], it was found here for the first time that the addition of divalent calcium salt induced stacking of the NCP-145 into columns packed in a hexagonal lattice, caused by the dominance of the attractive forces originating from ion-ion correlations and tail-bridging at sufficiently high salt concentration. In the presence of both Mg^{2+} and Ca^{2+}, linker DNA suppressed the alignment between the columns of stacked NCP-177, as it may act as the charged brush preventing the formation of the columnar hexagonal phase due to both steric obstacle and electrostatic repulsion. In other words, although in the case of both NCP-145 and NCP-177, the addition of divalent ions resulted in the formation of a turbid solutions forming a precipitate, only the NCP-145 system exhibits the ordered columnar phase while the precipitated phase of NCP-177 most likely corresponds to the one with limited but small degree of stacking in small clusters of NCP columns.

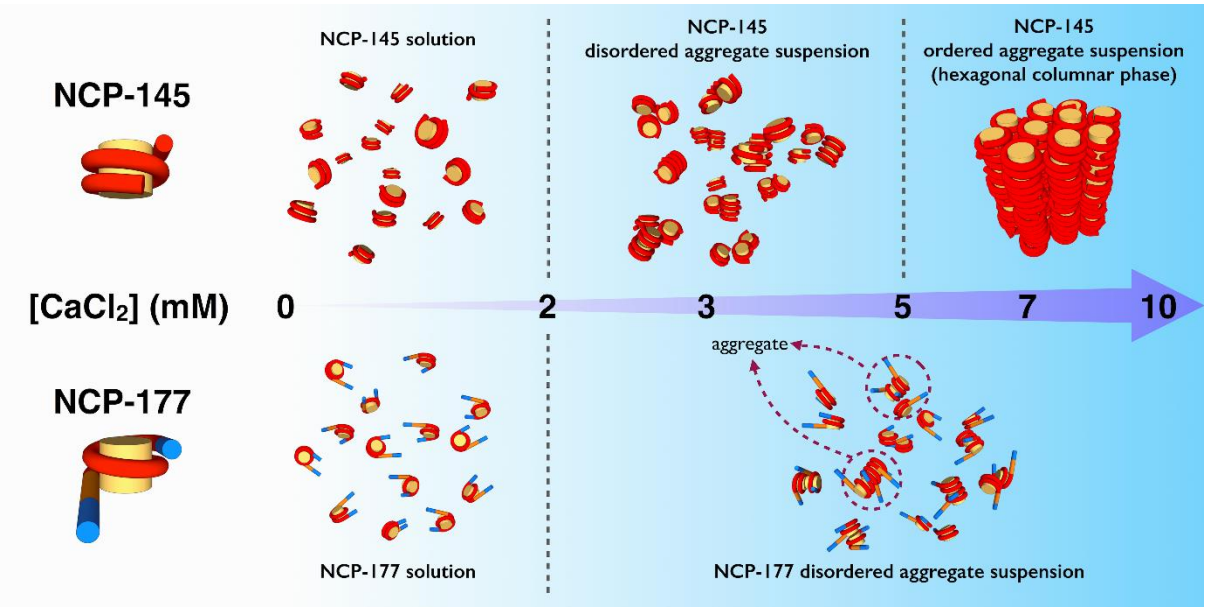

Fig. 6. The schematic illustration of the divalent calcium-salt effect on the structure of the nucleosome systems.

Acknowledgments

This work was supported by a Singapore Ministry of Education Academic Research Fund (AcRF) through a Tier 3 grant (MOE2012-T3-1-001) and the Ministry of Science and Technology, Taiwan under grant No. MOST 105-2221-E-007-137-MY3. We are indebted to the National Synchrotron Radiation Research Center (NSRRC) for synchrotron beamtime.

References

1. R. D. Kornberg and Y. Lorch, *Cell*, 1999, **98**, 285-294.
2. K. Luger, A. W. Mader, R. K. Richmond, D. F. Sargent and T. J. Richmond, *Nature*, 1997, **389**, 251-260.
3. C. A. Davey, D. F. Sargent, K. Luger, A. W. Maeder and T. J. Richmond, *J. Mol. Biol.*, 2002, **319**, 1097-1113.
4. R. K. McGinty and S. Tan, *Chem. Rev.*, 2015, **115**, 2255-2273.
5. A. R. Cutter and J. J. Hayes, *FEBS Lett.*, 2015, **589**, 2914-2922.
6. K. Luger and T. J. Richmond, *Curr.Opin.Genet.Dev.*, 1998, **8**, 140-146.
7. J. C. Hansen, C. Tse and A. P. Wolffe, *Biochemistry*, 1998, **37**, 17637-17641.
8. K. Luger, M. L. Dechassa and D. J. Tremethick, *Nat. Rev. Mol. Cell Biol.*, 2012, **13**, 436-447.
9. G. Felsenfeld and M. Groudine, *Nature*, 2003, **421**, 448-453.
10. J. O. Thomas, *Curr.Opin.Cell Biol.*, 1999, **11**, 312-317.

11. P. J. J. Robinson, L. Fairall, V. A. T. Huynh and D. Rhodes, *Proc. Natl. Acad. Sci. U.S.A.*, 2006, **103**, 6506-6511.
12. F. Song, P. Chen, D. Sun, M. Wang, L. Dong, D. Liang, K.-M. Xu, P. Zhu and C. Li, *Science*, 2014, **344**, 376-380.
13. A. Routh, S. Sandin and D. Rhodes, *Proc. Natl. Acad. Sci. U.S.A.*, 2008, **105**, 8872-8877.
14. N. Naumova, M. Imakaev, G. Fudenberg, Y. Zhan, B. R. Lajoie, L. A. Mirny and J. Dekker, *Science*, 2013, **342**, 948-953.
15. Y. Nishino, M. Eltsov, Y. Joti, K. Ito, H. Takata, Y. Takahashi, S. Hihara, A. S. Frangakis, N. Imamoto, T. Ishikawa and K. Maeshima, *EMBO J.*, 2012, **31**, 1644–1653.
16. J. B. Rattner and B. A. Hamkalo, *J. Cell. Biol.*, 1979, **81**, 453-457.
17. C. L. Woodcock, *J. Cell. Biol.*, 1994, **125**, 11-19.
18. N. Korolev, O. V. Vorontsova and L. Nordenskiöld, *Prog. Biophys. Mol. Biol.*, 2007, **95**, 23-49.
19. N. Korolev, A. Allahverdi, A. P. Lyubartsev and L. Nordenskiöld, *Soft Matter*, 2012, **8**, 9322–9333.
20. S. Mangenot, E. Raspaud, C. Tribet, L. Belloni and F. Livolant, *Eur.Phys.J.E*, 2002, **7**, 221-231.
21. A. Bertin, A. Leforestier, D. Durand and F. Livolant, *Biochemistry*, 2004, **43**, 4773-4780.
22. F. Gordon, K. Luger and J. C. Hansen, *J. Biol. Chem.*, 2005, **280**, 33701-33706.
23. A. Bertin, M. Renouard, J. S. Pedersen, F. Livolant and D. Durand, *Biophys. J.*, 2007, **92**, 2633-2645.
24. N. Korolev, A. P. Lyubartsev and L. Nordenskiöld, *Biophys. J.*, 2006, **90**, 4305-4316.
25. R. Buning and J. van Noort, *Biochimie*, 2010, **92**, 1729-1740.
26. G. Almouzni and H. Cedar, *Cold Spring Harb. Perspect. Biol.*, 2016, **8**, doi: 10.1101/cshperspect.a019372.
27. S. Ramachandran, K. Ahmad and S. Henikoff, *Mol. Cell*, 2017, **68**, 1038-1053.e1034.
28. F. T. Chien and J. van Noort, *Curr. Pharm. Biotechnol.*, 2009, **10**, 474-485.
29. M. G. Poirier, M. Bussiek, J. Langowski and J. Widom, *J.Mol.Biol.*, 2008, **379**, 772-786.
30. F. Livolant, S. Mangenot, A. Leforestier, A. Bertin, M. de Frutos, E. Raspaud and D. Durand, *Philos. Trans. A Math. Phys. Eng. Sci.*, 2007, **364**, 2615-2633.
31. N. V. Berezhnoy, Y. Liu, A. Allahverdi, R. Yang, C.-J. Su, C.-F. Liu, N. Korolev and L. Nordenskiöld, *Biophys. J.*, 2016, **110**, 1720–1731.
32. Y. Yang, A. P. Lyubartsev, N. Korolev and L. Nordenskiöld, *Biophys. J.*, 2009, **96**, 2082-2094.
33. H. Schiessel, *Eur. Phys. J. E*, 2006, **19**, 251-262.
34. Y. Fan, N. Korolev, A. P. Lyubartsev and L. Nordenskiöld, *PLoS One*, 2013, **8**, e54228.
35. A. P. Lyubartsev, N. Korolev, Y. Fan and L. Nordenskiöld, *J. Phys. Condens. Matter*, 2015, **27**, 064111.
36. S. Mangenot, A. Leforestier, P. Vachette, D. Durand and F. Livolant, *Biophys. J.*, 2002, **82**, 345-356.
37. A. Bertin, S. Mangenot, M. Renouard, D. Durand and F. Livolant, *Biophys.J.*, 2007, **93**, 3652-3663.
38. S. C. Howell, K. Andresen, I. Jimenez-Useche, C. Yuan and X. Qiu, *Biophys. J.*, 2013, **105**, 194-199.
39. M. de Frutos, E. Raspaud, A. Leforestier and F. Livolant, *Biophys. J.*, 2001, **81**, 1127-1132.
40. Y. Liu, C. Lu, Y. Yang, Y. Fan, R. Yang, C.-F. Liu, N. Korolev and L. Nordenskiöld, *J.*

Mol. Biol., 2011, **414**, 749–764.
41. J. C. Hansen, *Annu. Rev. Biophys. Biomol. Struct.*, 2002, **31**, 361-392.
42. A. Zinchenko, N. V. Berezhnoy, S. Wang, W. M. Rosencrans, N. Korolev, J. R. C. van der Maarel and L. Nordenskiöld, *Nucleic Acids Res.*, 2018, **46**, 635-649.
43. A. Zinchenko, N. V. Berezhnoy, Q. Chen and L. Nordenskiöld, *Biophys. J.*, 2018, **114**, 2326-2335.
44. N. Korolev, A. P. Lyubartsev and L. Nordenskiöld, *Adv. Colloid Interface Sci.*, 2010, **158**, 32–47.
45. C. Yang, M. J. van der Woerd, U. M. Muthurajan, J. C. Hansen and K. Luger, *Nucleic Acids Res.*, 2011, **39**, 4122-4135.
46. Y. Arimura, H. Kimura, T. Oda, K. Sato, A. Osakabe, H. Tachiwana, Y. Sato, Y. Kinugasa, T. Ikura, M. Sugiyama, M. Sato and H. Kurumizaka, *Sci. Rep.*, 2013, **3**, 3510.
47. I. Jimenez-Useche, J. Ke, Y. Tian, D. Shim, S. C. Howell, X. Qiu and C. Yuan, *Sci. Rep.*, 2013, **3**, 2121.
48. K. Andresen, I. Jimenez-Useche, S. C. Howell, C. Yuan and X. Qiu, *PLoS One*, 2013, **8**, e78587.
49. A. Bertin, D. Durand, M. Renouard, F. Livolant and S. Mangenot, *Eur.Biophys.J.*, 2007, **36**, 1083-1094.
50. J. T. Finch, L. C. Lutter, D. Rhodes, R. S. Brown, B. Rushton, M. Levitt and A. Klug, *Nature*, 1977, **269**, 29-36.
51. D. Vasudevan, E. Y. Chua and C. A. Davey, *J.Mol.Biol.*, 2010, **403**, 1-10.
52. T. Schalch, S. Duda, D. F. Sargent and T. J. Richmond, *Nature*, 2005, **436**, 138-141.
53. B. Dorigo, T. Schalch, A. Kulangara, S. Duda, R. R. Schroeder and T. J. Richmond, *Science*, 2004, **306**, 1571-1573.
54. M. P. Scheffer, M. Eltsov, J. Bednar and A. S. Frangakis, *J.Struct.Biol.*, 2012, **178**, 207-214.
55. P. Castro-Hartmann, M. Milla and J.-R. Daban, *Biochemistry*, 2010, **49**, 4043-4050.
56. N. Korolev, A. P. Lyubartsev and L. Nordenskiöld, *Sci. Rep.*, 2018, **8**, 1543.
57. P. J. J. Robinson, W. An, A. Routh, F. Martino, L. Chapman, R. G. Roeder and D. Rhodes, *J. Mol. Biol.*, 2008, **381**, 816-825.
58. S. J. Correll, M. H. Schubert and S. A. Grigoryev, *EMBO J.*, 2012, **31**, 2416-2426.
59. R. Buning, W. Kropff, K. Martens and J. van Noort, *J. Phys. Condens. Matter*, 2015, **27**, 064103.
60. W. J. A. Koopmans, R. Buning, T. Schmidt and J. van Noort, *Biophys. J.*, 2009, **97**, 195-204.
61. P. T. Lowary and J. Widom, *J. Mol. Biol.*, 1998, **276**, 19-42.
62. R. A. Rogge, A. A. Kalashnikova, U. M. Muthurajan, M. E. Porter-Goff, K. Luger and J. C. Hansen, *J. Vis. Exp.*, 2013, **79**, e50354.
63. K. Luger, T. J. Rechsteiner and T. J. Richmond, *Methods Enzymol.*, 1999, **304**, 3-19.
64. K. Luger, T. Rechsteiner and T. J. Richmond, *Methods Mol.Biol.*, 1999, **119**, 1-16.
65. P. N. Dyer, R. S. Edayathumangalam, C. L. White, Y. Bao, S. Chakravarthy, U. M. Muthurajan and K. Luger, *Methods Enzymol.*, 2004, **375**, 23-44.
66. U.-S. Jeng, C. H. Su, C.-J. Su, K.-F. Liao, W.-T. Chuang, Y.-H. Lai, J.-W. Chang, Y.-J. Chen, Y.-S. Huang, M.-T. Lee, K.-L. Yu, J.-M. Lin, D.-G. Liu, C.-F. Chang, C.-Y. Liu, C.-H. Changa and K. S. Liang, *J. Appl. Cryst.*, 2010, **43**, 110-121.
67. M. V. Petoukhov, D. Franke, A. V. Shkumatov, G. Tria, A. G. Kikhney, M. Gajda, C. Gorba, H. D. T. Mertens, P. V. Konarev and D. I. Svergun, *J. Appl. Crystallogr.*, 2012, **45**, 342-350.
68. D. Franke, M. V. Petoukhov, P. V. Konarev, A. Panjkovich, A. Tuukkanen, H. D. T.

Mertens, A. G. Kikhney, N. R. Hajizadeh, J. M. Franklin, C. M. Jeffries and D. I. Svergun, *J. Appl. Crystallogr.*, 2017, **50**, 1212-1225.
69. J. Trewhella, A. P. Duff, D. Durand, F. Gabel, J. M. Guss, W. A. Hendrickson, G. L. Hura, D. A. Jacques, N. M. Kirby, A. H. Kwan, J. Pérez, L. Pollack, T. M. Ryan, A. Sali, D. Schneidman-Duhovny, T. Schwede, D. I. Svergun, M. Sugiyama, J. A. Tainer, P. Vachette, J. Westbrook and A. E. Whitten, *Acta Crystallogr. D Struct. Biol.*, 2017, **73(Pt 9)**, 710-728.
70. T. Macke and D. A. Case, in *Molecular Modeling of Nucleic Acids*, eds. N. B. Leontes and J. SantaLucia, Washington, DC, 1998, pp. 379-393.
71. E. F. Pettersen, T. D. Goddard, C. C. Huang, G. S. Couch, D. M. Greenblatt, E. C. Meng and T. E. Ferrin, *J. Comp. Chem.*, 2004, **25**, 1605-1612.
72. J. P. Hansen and J. B. Hayter, *Mol. Phys.*, 1982, **46**, 651-656.
73. S. R. Kline, *J. Appl. Crystallogr.*, 2006, **39**, 895-900.
74. Y. Chen, J. M. Tokuda, T. Topping, J. L. Sutton, S. P. Meisburger, S. A. Pabit, L. M. Gloss and L. Pollack, *Nucleic Acids Res.*, 2014, **42**, 8767-8776.
75. Y. Chen, J. M. Tokuda, T. Topping, S. P. Meisburger, S. A. Pabit, L. M. Gloss and L. Pollack, *Proc. Natl. Acad. Sci. U.S.A.*, 2017, **114**, 334-339.
76. T. J. Richmond and C. A. Davey, *Nature*, 2003, **423**, 145-150.
77. F. Zhang, M. W. A. Skoda, R. M. J. Jacobs, R. A. Martin, C. M. Martin and F. Schreiber, *J. Phys. Chem. B*, 2007, **111**, 251-259.
78. J. B. Hayter and J. Penfold, *Mol. Phys.*, 1981, **42**, 109-118.
79. K. Maeshima, R. Rogge, S. Tamura, Y. Joti, T. Hikima, H. Szerlong, C. Krause, J. Herman, E. Seidel, J. DeLuca, T. Ishikawa and J. C. Hansen, *EMBO J.*, 2016, **35**, 1115–1132.
80. N. Korolev, Y. Zhao, A. Allahverdi, K. D. Eom, J. P. Tam and L. Nordenskiöld, *Biochem. Biophys. Res. Comm.*, 2012, **418**, 205-210.
81. A. Allahverdi, Q. Chen, N. Korolev and L. Nordenskiöld, *Sci. Rep.*, 2015, **5**, 8512.
82. N. Korolev, A. Allahverdi, Y. Yang, Y. Fan, A. P. Lyubartsev and L. Nordenskiöld, *Biophys. J.*, 2010, **99** 1896-1905.
83. R. Phengchat, H. Takata, K. Morii, N. Inada, H. Murakoshi, S. Uchiyama and K. Fukui, *Sci. Rep.*, 2016, **6**, 38281.
84. Z. Yang and J. J. Hayes, *Biochemistry*, 2011, **50**, 9973-9981.

TOC Graphic

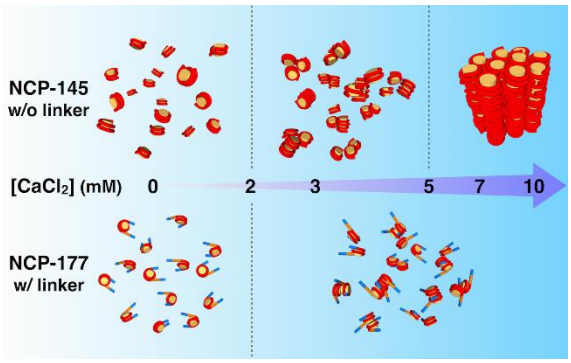

Small angle X-ray scattering reveals partial unwrapping of nucleosomal DNA on the nucleosome core particle (NCP) composed of linker DNA of 30 bp or less, and the linker DNA alleviates the electrostatic repulsion between the NCPs and prevents the formation of ordered columnar hexagonal phase, demonstrating that linker DNA plays an active role in chromatin folding.

SUPPLEMENTARY INFORMATION

The Effect of Linker DNA on the Structure and Interaction of Nucleosome Core Particles

Yen-Chih Huang, Chun-Jen Su, Nikolay Korolev, Nikolay V. Berezhnoy, Sai Wang, Aghil Soman, Chun-Yu Chen, Hsin-Lung Chen, U-Ser Jeng, and Lars Nordenskiöld

DNA sequences used in nucleosome reconstitutions.
145 bp 601, (net charge –288e):

TGGAGAATCC CGGTGCCGAG GCCGCTCAAT TGGTCGTAGA CAGCTCTAGC ACCGCTTAAA CGCACGTACG CGCTGTCCCC CGCGTTTTAA CCGCCAAGGG GATTACTCCC TAGTCTCCAG GCACGTGTCA GATATATACA TCCTG
157 bp, (net charge –312e):

ACTCCC **--- 145bp 601 ---** TGCAGT
177 bp, (net charge –352e):

ACTTACGCGG CCGCCC **--- 145bp 601 ---** TGCATGTATT GAAAGT
601-207; net charge -412e

ATCTCGGGGA TGGACCCTAT ACGCGGCCGC CC **--- 145bp 601 ---** TGCATGTATT GAACAGCGAC CTCTCGGGAT

Fig. S1. Polyacrylamide gel electrophoretograms of nucleosomes with 145, 157, 177 and 207

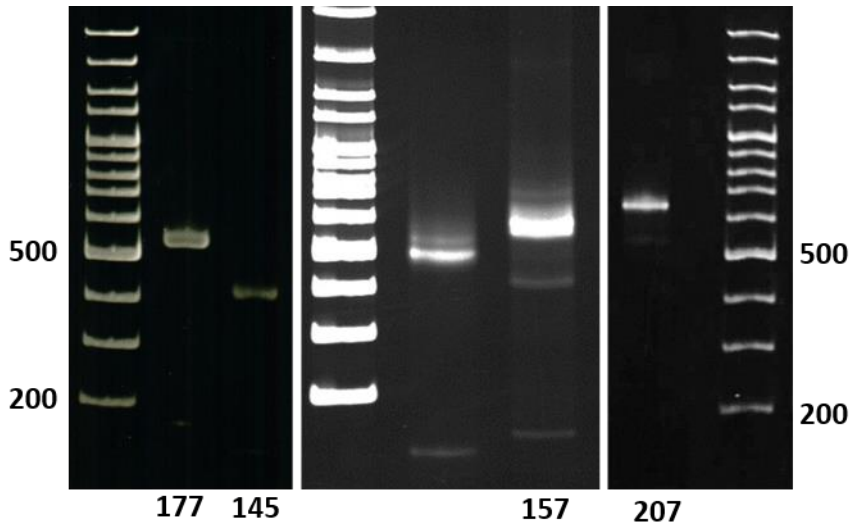

bp DNA. The 100 bp DNA marker ladder with 500 bp and 200 bp DNA fragments are indicated for reference. The unlabeled middle lane in the middle panel is NCP-145 with a different DNA sequence not studied in this work. The figure was assembled from three gels that were run separately, imaged and cropped to show the areas of interest. The original gel images are available upon request.

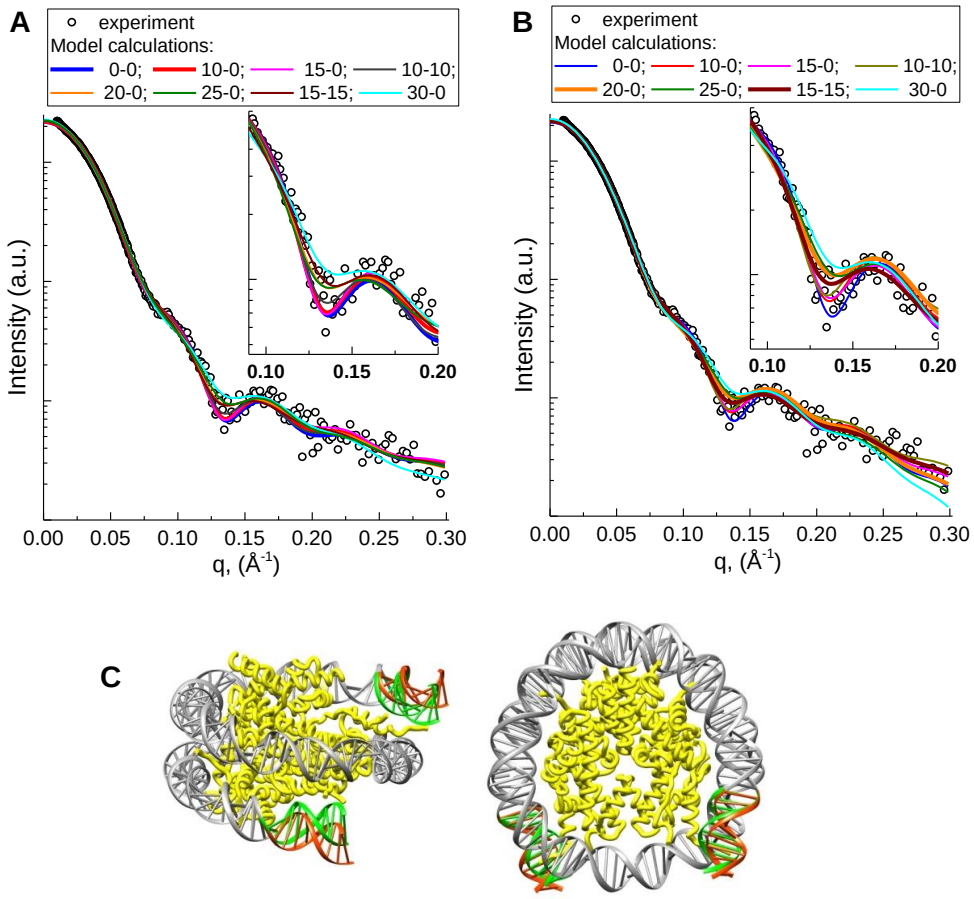

Figure S2. Comparison of SAXS spectra measured in experiment (points) and simulated from molecular structures (curves). Experimental data are for the NCP-145 (1.25 mg/mL). Curves show the SAXS profiles calculated from the molecular structures modelling different degrees of unwinding from one or two ends of the NCPs as indicated in the legend above the graphs. Calculated SAXS profiles were determined using two different NCP structures: (**A**) A snapshot from the MD simulations with histone tails collapsed on the DNA was used as initial structure to build models with DNA unwrapping. **(B).** 145 bp with '601' DNA sequence (3LZ0.pdb (1); histone source and DNA sequence are similar to the ones used in experiment but with significant number of the amino acids from the histone tails missing from the structure). Inserts in (A) and (B) show superimposed experimental SAXS spectra to highlight the local minimum at q = 0.14 $Å^{-1}$. **(C).** An illustration that unwrapping of 10 bp DNA from each end of the NCP-145 results in relatively small alteration of the nucleosome structure.

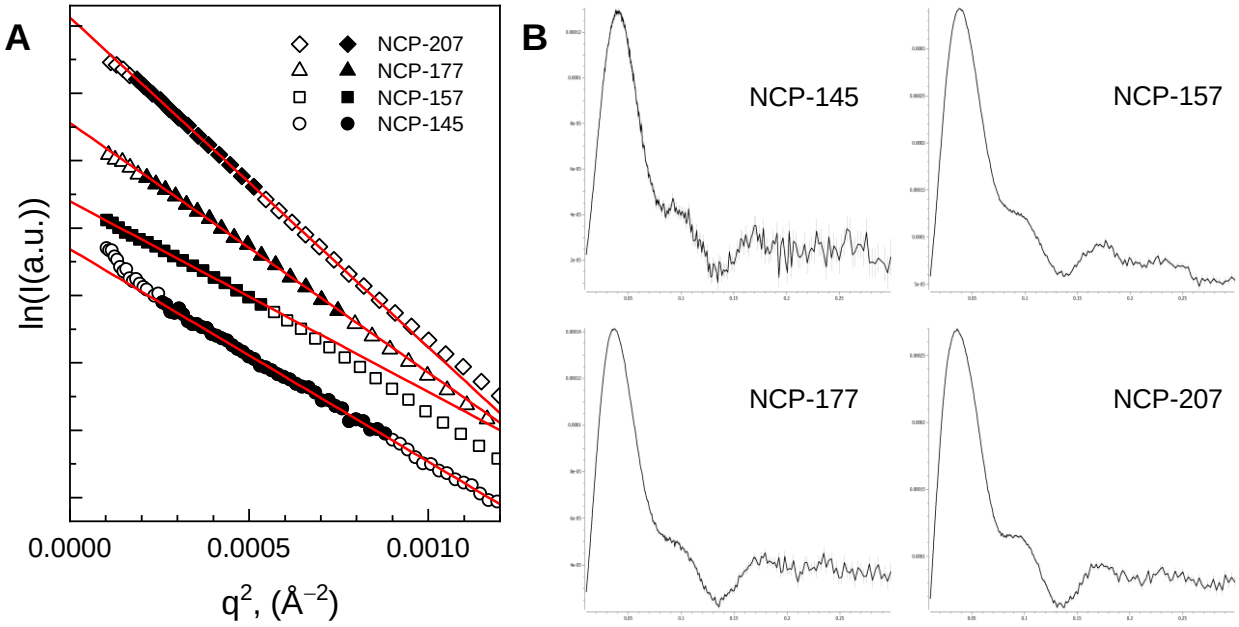

Figure S3. Examples of Guinier (**A**) and Kratky (**B**) plots calculated from the SAXS spectra of the nucleosome solutions shown in Fig. 1 of the main text (NCP-145, 1.25 mg/mL; NCP-157, 3 mg/mL; NCP-177, 1.5 mg/mL; and NCP-207, 3 mg/mL). In (**A**) solid points used for linear fitting shown by red lines; Rg values calculated from the Guinier plots are given in Tables S1-S4. In (**B**) four panels are output from the ATSAS software with identity of the NCP sample indicated in the panels. Bell-shaped form of all curves indicates that all samples of the NCP are folded and globular.

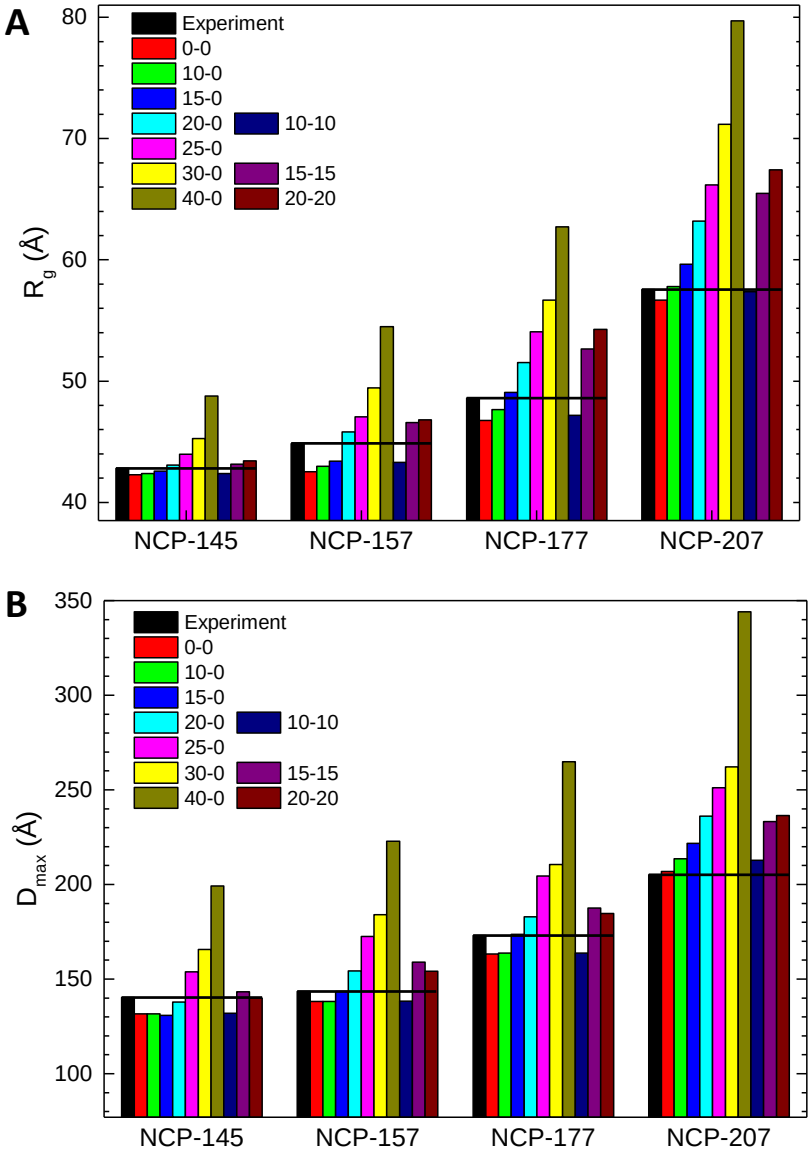

Figure S4. Comparison of the R_g (**A**) and D_{max} (**B**) values calculated from the SAXS solution spectra (in black) with the corresponding values from the form factor profiles (in colours) obtained for the atomic structures modelling DNA unwrapping from the histone octamer. The simulated data is grouped according to the number of DNA base pairs unwrapped in asymmetric (from one end) or symmetric fashion (from two ends). To guide an eye, horizontal lines are drawn on the levels of the experimental R_g and D_{max} values. In (**A**) and (**B**) origins of the y-axis are placed at position of the respective radius and diameter of the sphere with volume equal to the all-atom volume of the dry NCP-145 that corresponds to the minimal possible R_g (38.5 Å) and D_{max} (77 Å) values for all nucleosome structures.

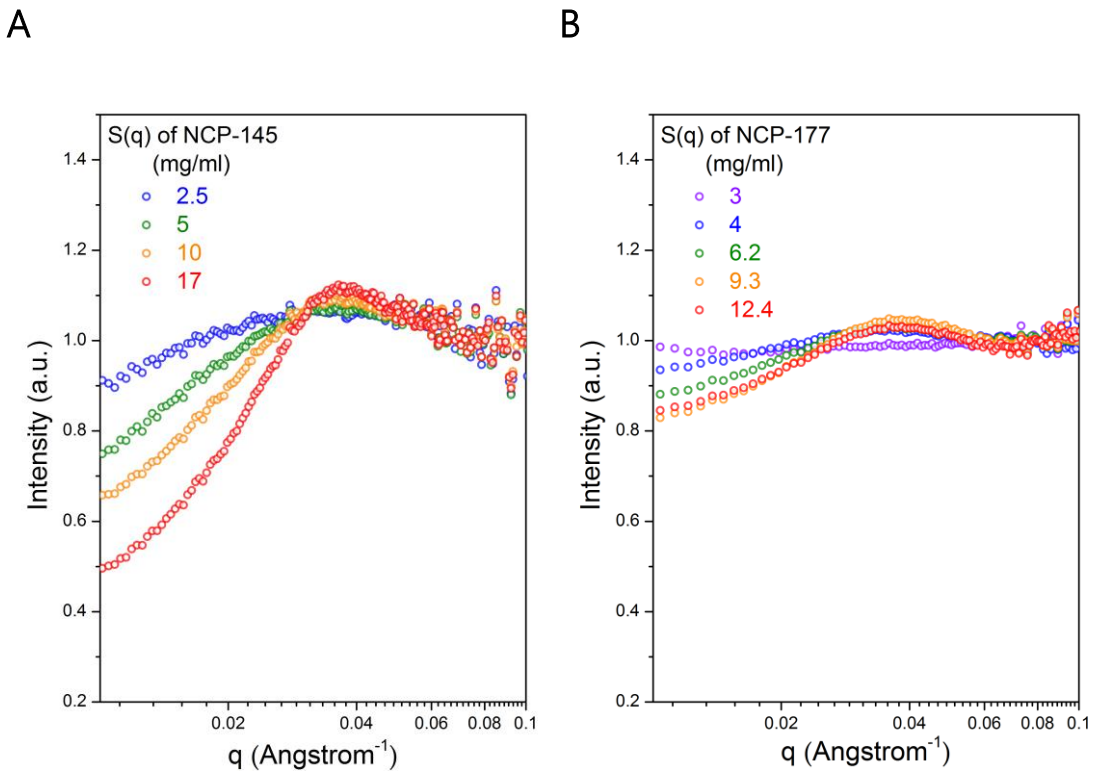

Figure S5. The structure factors, *S(q)*, of NCP-145(A) and NCP-177(B) at various concentrations obtained by dividing the intensity profiles by their respective form factors. Over the concentration range studied, the structure factor of NCP-145 displayed a much more pronounced concentration dependence and deviation from the value of 1.0 in the low-q region than that of NCP-177, conforming that NCP-145 exhibited a stronger interparticle interaction than NCP-177 under a given concentration.

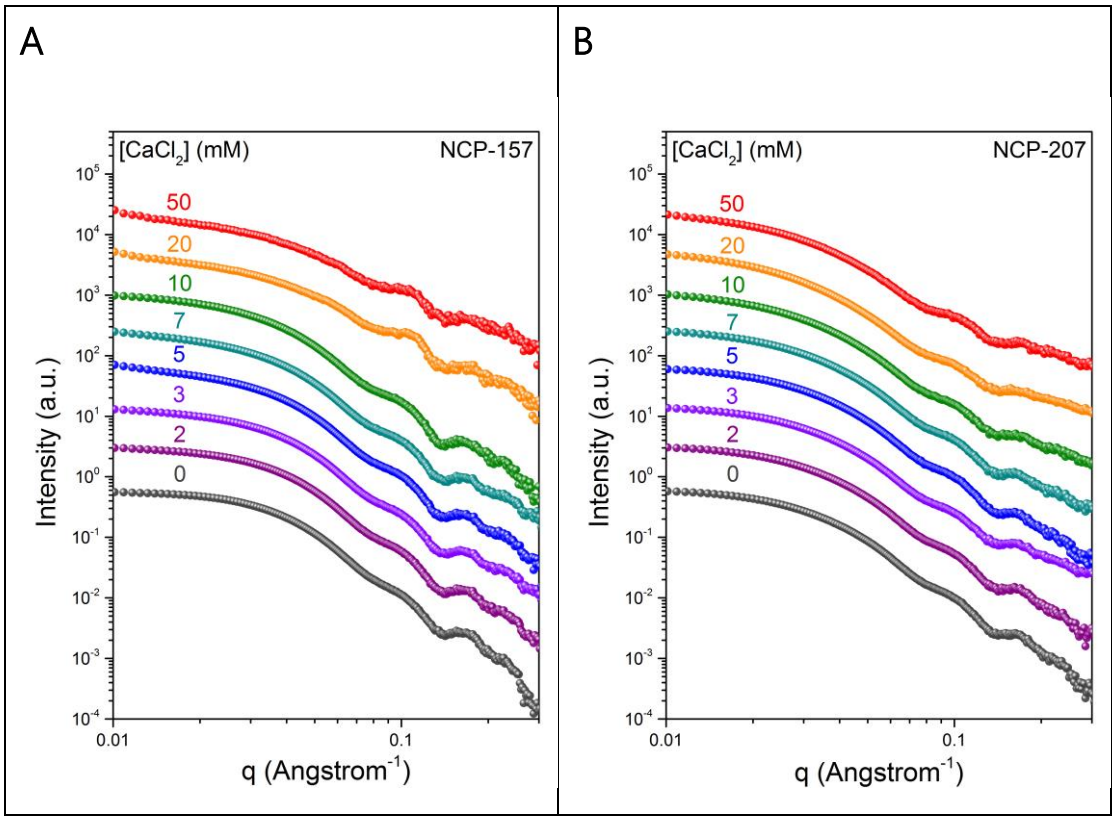

Figure S6. Influence of $CaCl_2$ on the structures and interparticle interactions of the NCP-157(A) and NCP-207 (B). Concentrations of added $CaCl_2$ (in mM) are indicated in the graphs. The initial NCP concentrations are 2.5 and 3 mg/ml for NCP-157 and NCP-207, respectively.

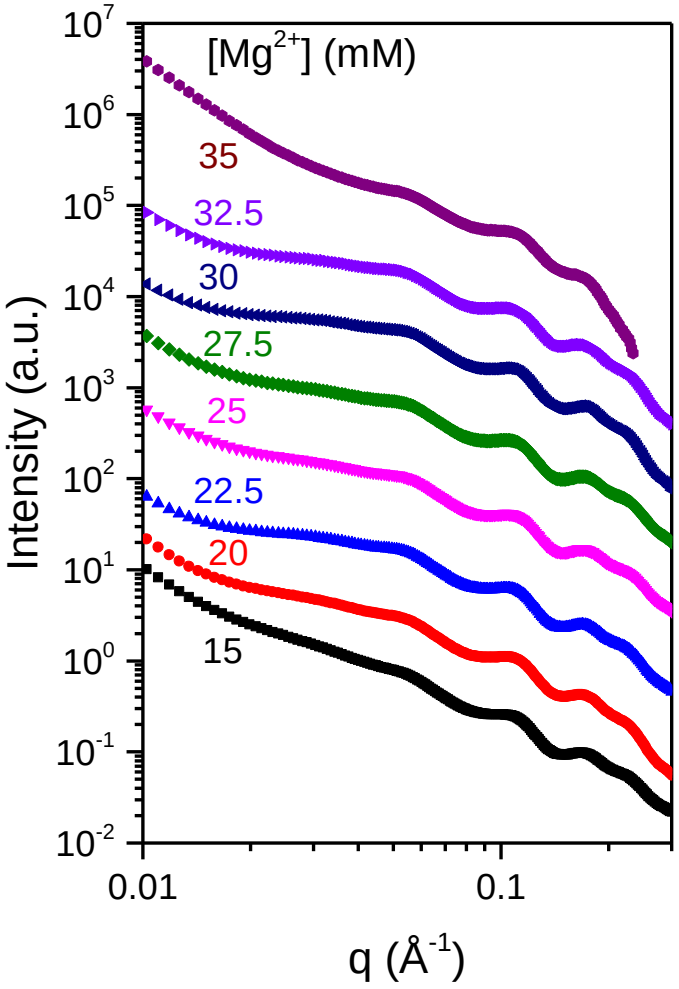

Figure S7. SAXS spectra of NCP-177 at 8 mg/mL precipitated by Mg^{2+}. Concentrations of Mg^{2+} are indicated next to the corresponding spectrum of the same color.

Table S1. Comparison of the outputs from SAXS profiles obtained the NCP-145 in experiment and simulated from modelled molecular structures, including the radius of gyration *(R_g)* and the maximal intra-atom distances within a particle (D_{max}) determined from the distance distribution function *P(r)*. Top row of numbers shows parameters obtained from the experiment; two sections below present output of the analysis of molecular structures constructed from stretches of straight DNA and crystal structure 1KX5.

Number of unwrapped bp	R_g from Guinier plot, Å	R_g from P(r), Å	D_{max}, Å	Fit quality*, χ^2
Data extracted from SAXS measurement NCP-145, 1.25 mg/mL				
	42.85 +/– 0.22	**42.80** +/– 0.15	**140.2**	0.952 excellent
Structure with collapsed tails generated MD simulations using 1KX5 coordinates				
0-0	42.49	42.29	131.6	**2.12**
10-0	42.59	42.38	131.7	**2.10**
15-0	42.76	42.58	130.8	**2.16**
10-10	42.56	42.37	131.9	**2.14**
20-0	43.26	43.08	137.8	2.33
25-0	44.10	43.96	153.8	2.60
15-15	43.31	43.14	143.3	2.60
30-0	45.33	45.26	165.6	3.16
20-20	43.54	43.43	140.0	2.79
40-0	48.76	48.77	199.2	6.62
Crystal structure 3LZ0 with '601' DNA sequence				
0-0	41.42	41.43	117.0	4.68
10-0	41.91	41.92	121.5	2.88
15-0	42.08	42.09	125.5	2.63
10-10	42.14	42.18	122.4	2.84
20-0	43.08	43.11	139.9	**2.10**
25-0	43.57	43.62	145.8	2.42
15-15	42.58	42.61	127.5	**2.10**
30-0	45.06	45.16	159.9	3.00
20-20	44.14	44.28	153.2	3.24
40-0	50.09	50.40	199.9	9.51

*For the experimental data, fit quality value represents the pair distance distribution fit from the GNOM module of the ATSAS package. For the NCP models, the fit quality is defined by χ^2 value calculated for the difference between experimental and simulated spectra.

Table S2. Comparison of output from SAXS profiles obtained the NCP-157 in experiment and simulated from modelled molecular structures, including the radius of gyration *(R_g)* and the maximal intra-atom distances within a particle (D_{max}) determined from the distance distribution function *P(r)*.. Top row of numbers shows parameters obtained from the experiment; a section below presents output of the analysis of molecular structures constructed from stretches of straight DNA and MD-generated NCP-145 structure.

Number of unwrapped bp	R_g from Guinier plot, Å	R_g from P(r), Å	D_{max}, Å	Fit quality*, χ^2
NCP-157; 3.0 mg/mL; data extracted from SAXS profile				
	44.86 +/– 0.63	**44.85** +/– 0.63	**143.5**	0.669 reasonable
Structures generated by combining MD-generated NCP and straight B-DNA fragments				
0-0	42.59	42.52	138.2	32.09
10-0	43.01	42.97	138.2	33.17
15-0	43.46	43.41	143.4	35.99
10-10	43.35	43.29	138.4	44.81
20-0	45.88	45.80	154.3	32.41
25-0	47.06	47.05	172.6	9.87
15-15	46.69	46.57	158.9	38.27
30-0	49.35	49.43	184.1	**4.61**
20-20	46.80	46.80	154.1	37.89
40-0	54.21	54.48	222.9	8.81

*For the experimental data, fit quality value represents the pair distance distribution fit from the GNOM module of the ATSAS package. For the NCP models, the fit quality is defined by χ^2 value calculated for the difference between experimental and simulated spectra

Table S3. Comparison of output from SAXS profiles obtained the NCP-177 in experiment and simulated from modelled molecular structures, including the radius of gyration *(R_g)* and the maximal intra-atom distances within a particle (D_{max}) determined from the distance distribution function *P(r)*. Top row of numbers shows parameters obtained from the experiment; a section below presents output of the analysis of molecular structures constructed from stretches of straight DNA and MD-generated NCP-145 structure.

Number of unwrapped bp	R_g from Guinier plot, Å	R_g from P(r), Å	D_{max}, Å	Fitting quality*, χ^2
NCP-177; 1.5 mg/mL; data extracted from SAXS profile				
	48.57 +/– 0.30	**48.60** +/– 0.30	**173.0**	0.783 good
Structures generated by combining MD-generated NCP and straight B-DNA fragments				
0-0	46.69	46.75	163.2	**2.20**
10-0	47.61	47.65	163.7	**3.50**
15-0	49.04	49.06	173.7	5.79
10-10	47.08	47.17	163.7	5.78
20-0	51.42	51.52	182.9	15.19
25-0	53.86	54.07	204.4	7.16
15-15	52.52	52.66	187.5	14.57
30-0	56.36	56.69	210.6	9.47
20-20	54.05	54.26	184.6	12.24
40-0	62.31	62.72	264.8	11.05

*For the experimental data, fit quality value represents the pair distance distribution fit from the GNOM module of the ATSAS package. For the NCP models, the fit quality is defined by χ^2 value calculated for the difference between experimental and simulated spectra

Table S4. Comparison of output from SAXS profiles obtained the NCP-207 in experiment and simulated from modelled molecular structures, including the radius of gyration *(R_g)* and the maximal intra-atom distances within a particle (D_{max}) determined from the distance distribution function *P(r)*.. Top row of numbers shows parameters obtained from the experiment; a section below presents output of the analysis of molecular structures constructed from stretches of straight DNA and MD-generated NCP-145 structure.

Number of unwrapped bp	R_g from Guinier plot, Å	R_g from P(r), Å	D_{max}, Å	Fit quality*, χ^2
NCP-207; 3.0 mg/mL; data extracted from SAXS profile				
	54.18 +/– 0.59	**57.54** +/– 0.08	**205.1**	0.695 reasonable
Structures generated by combining MD-generated NCP and straight B-DNA fragments				
0-0	56.25	56.69	206.8	**5.04**
10-0	57.42	57.80	213.6	6.91
15-0	59.14	59.63	221.8	9.61
10-10	57.00	57.38	212.8	51.67
20-0	62.63	63.20	236.1	78.44
25-0	65.48	66.17	251.1	23.07
15-15	64.79	65.47	233.2	25.80
30-0	70.46	71.18	262.2	13.93
20-20	66.60	67.42	236.5	14.80
40-0	78.86	79.71	344.1	24.12

*For the experimental data, fit quality value represents the pair distance distribution fit from the GNOM module of the ATSAS package. For the NCP models, the fit quality is defined by χ^2 value calculated for the difference between experimental and simulated spectra.

Table S5. Analysis of SAXS solution spectra obtained for NCP-145 and NCP-177 at different NCP concentrations

Concentration, mg/mL:	R_g from Guinier plot, Å	R_g from P(r), Å	D_{max}, Å	Fit quality*
NCP-145				
1.25	42.85 +/– 0.22	42.80 +/– 0.22	140.2	0.952 excellent
2.5	41.84 +/– 0.48	41.71+/–0.48	119.1	0.878, good
5.0	41.83 +/– 1.08	41.71+/–1.08	121.3	0.684, reasonable
10.0	41.65+/– 2.19	41.53+/– 2.19	117.8	0.679, reasonable
17.0	--	--	--	No solution
NCP-177				
1.5	48.57 +/– 0.30	48.60 +/– 0.30	173.0	0.783 good
3.0	47.79 +/– 0.61	47.80+/– 0.61	156.6	0.655, reasonable
4.0	47.60+/– 0.88	47.61+/– 0.88	156.1	0.657, reasonable
6.2	46.85+/–1.41	46.83+/– 1.41	151.6	0.660, reasonable
9.3	46.00+/–2.28	45.96+/– 2.28	146.0	0.663, reasonable
12.4	46.13+/– 2.81	46.09+/– 2.81	146.6	0.664, reasonable

*For the experimental data, fit quality value represents the pair distance distribution fit from the GNOM module of the ATSAS package.

Supporting References

1. Vasudevan, D., Chua, E.Y. and Davey, C.A. (2010) Crystal structures of nucleosome core particles containing the '601' strong positioning sequence. *J.Mol.Biol.*, **403**, 1-10.